

pubs.acs.org/Macromolecules Article

# **Conformational Statistics of Ribbon-like Chains**

Wesley Michaels,\* Andrew J. Spakowitz, and Jian Qin\*



Cite This: Macromolecules 2023, 56, 8359-8368



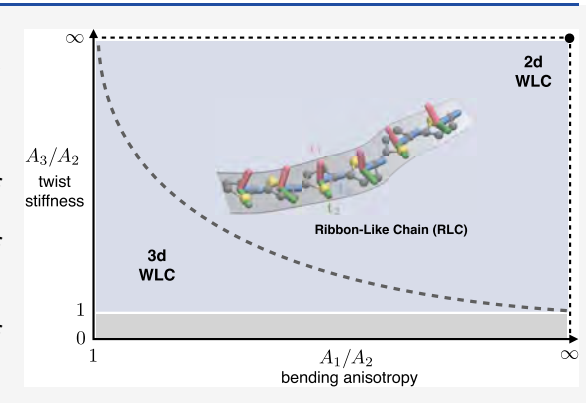
**ACCESS** I

Metrics & More

Article Recommendations

s Supporting Information

ABSTRACT: The chemistry of conjugated polymers and ladder polymers endows them with anisotropic bending stiffnesses in their backbones, giving rise to "ribbon-like" structures that the existing statistical polymer models do not fully capture. Here, we analyze a generalization to the worm-like chain (WLC) model, called the ribbon-like chain (RLC) model, which permits such conformational anisotropy and highlights the importance of backbone twisting stiffness. The free-chain Green function is solved, and the basic chain conformational properties are evaluated. The effects of anisotropic bending stiffness on the tangent and normal correlations, the radius of gyration, and the instantaneous chain shape are clearly revealed. Finally, parametrization, extension, and applications in the study of conjugated polymers are discussed.



## 1. INTRODUCTION

The worm-like chain (WLC) model of Kratky and Porod, representing the polymer chain as an inextensible string with a finite bending stiffness, has been widely used to capture the short-scale stiffness of real chains. The bending stiffness determines the persistence length and, in conjunction with the contour length, fully specifies the conformational properties of a single chain. Extensions to the WLC have been developed to capture twisting and finite extensibility of the backbone, and the helical worm-like chain (HWLC) model developed by Yamakawa and co-workers has successfully captured the finer local conformational variations of DNA and many synthetic polymers. These models incorporate chemical details such as backbones with rotatable bonds and sp³-hybridized carbon atoms to improve upon WLC predictions for polymers with these features.

In this work, we adopt the framework of the HWLC model and examine the conformational properties of ribbon-like chains (RLC). The RLC model is ideal for studying the conformations of conjugated polymers (CPs) and ladder polymers, which exhibit anisotropic bending stiffness and variable degrees of twisting stiffness. These features cannot be adequately captured by the standard family of WLC models. To demonstrate this, we consider polythiophene (Figure 1). Each monomer is assigned a triad of unit vectors (t<sub>1</sub>, t<sub>2</sub>, and  $\mathbf{t}_3$ ). The variation of chain conformation is decomposed into a combination of rotations about the triad: turning via rotation about the normal  $t_1$ , undulation via rotation about the binormal  $t_2$ , and twisting via rotation about the tangent  $t_3$ . Apparently, for CPs, the "undulating" mode is the typical bending, the in-plane "turning" mode is severely restricted, and the "twisting" mode is essential for out-of-plane deformation. For ladder polymers, the turning and twisting modes are suppressed, and the conformation statistics reduce to that for 2D WLC. The standard WLC model has isotropic bending stiffness. Therefore, the twisting mode is inconsequential and not needed. "Developable ribbons" are objects which can easily undulate and twist but not turn. As such, polymers exhibiting these tendencies have been described as "ribbon-like". <sup>6,7</sup>

The statistics of ribbon-like polymers have been considered in the past. Khokhlov and co-workers investigated the scaling behavior of polymers that bend freely in one plane yet are extremely rigid in the perpendicular direction, and studied the transition between uniaxial and biaxial nematic phases in such polymers. Golestanian, Liverpool, and Kremer adapted the "railway-track" model, which couples two WLCs with harmonic bonds, to study polymer ribbons via mean-field theory, perturbation theory, and Monte Carlo (MC) simulation. These studies have discussed the existence of kinks and twists in isolation, under confinement, or under compression. Arinstein developed a lattice model for ribbon-like polymers, which emphasized that, for noninteracting chains, anisotropies of polymer chains manifest more strongly in local conformational properties than macroscopic ordering.

Among these models, the HWLC model has incorporated most small-scale molecular feature and has been extensively treated.<sup>4</sup> It has isotropic bending moduli with a residual curvature and a twisting modulus. By introducing anisotropy

Received: July 18, 2023 Revised: September 15, 2023 Published: October 13, 2023





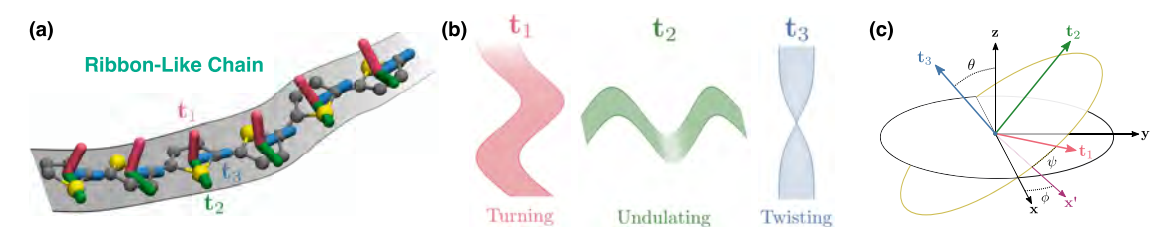


Figure 1. Schematic of ribbon-like chain. (a) Ball-and-stick model of a polythiophene oligomer (carbon in gray, sulfur in yellow, hydrogen not shown) with superimposed RLC tangent vectors ( $\mathbf{t}_1$  in red,  $\mathbf{t}_2$  in green,  $\mathbf{t}_3$  in blue) and a corresponding ribbon cartoon. (b) Three twisting modes available to the RLC: (left) "turning" via rotation about  $\mathbf{t}_1$ , (middle) "undulating" via rotation about  $\mathbf{t}_2$ , and (right) "twisting" via rotation about  $\mathbf{t}_3$ . (c) Euler angles  $\Omega = \{\phi, \theta, \psi\}$  defined in reference to the laboratory frame.

into the bending moduli and discarding the residual curvature, the model can be adapted for studying the conformation properties of the RLC. The Hamiltonian for the RLC is the same as that in the quantum mechanical treatment of the asymmetric rigid rotor, first developed for the spectroscopic analysis of polyatomic molecules. The trajectories of such rotors correspond to the conformations of the RLCs (Figure 1). Studies of ribbon-like polymer rings and twist-bend coupling in helical molecules 17–19 have applied this idea, but rely on approximations or perturbative analyses to develop conformational statistics.

Here, we present analytical results for the conformational properties of the RLC model. Akin to developments of the WLC, twistable WLC, and HWLC, in Section 2, we determine RLC statistics by casting the problem as a diffusion equation satisfied by the free-particle Green function. Following Yamakwa, the coefficients are evaluated for the series expansion of the Green function, which determines RLC conformational properties. In Section 3, we present the results on the tangent–tangent and normal–normal correlations,  $\langle R^2 \rangle$ , and  $\langle R_{\rm g}^2 \rangle$  for the RLC, and we discuss the influence of anisotropic bending on these properties. We further characterize the shape of RLCs by analyzing the statistics of aligned chains. In the concluding section, we discuss how the RLC model can be tested, applied, and extended.

## 2. RLC MODEL

We model the RLC as a continuous ribbon of fixed contour (centerline) length L. The position along the contour is denoted as s, with  $0 \le s \le L$ . Each segment s is assigned a triad of mutually orthogonal backbone vectors,  $\{\mathbf{t}_1, \ \mathbf{t}_2, \ \text{and} \ \mathbf{t}_3\}$  (Figure 1), with  $\mathbf{t}_3$  being the backbone tangent and  $\mathbf{t}_1$  and  $\mathbf{t}_2$  being the normal and binormal directions. The vectors  $\mathbf{t}_1$  and  $\mathbf{t}_2$  refer to the orientation of the *ribbon*, which should not be confused with the normal or binormal vectors of the *centerline*. It has been pointed out that the normal or binormal vectors of the centerline may rotate discontinuously, while  $\mathbf{t}_1$  or  $\mathbf{t}_2$  remains smooth. In general, the segmental orientation varies along the chain contour, and the vectors  $\mathbf{t}_i$  (i=1,2,3) are functions of s. To track conformational variation along the backbone, it is convenient to introduce the angular velocities  $\omega_i(s)$  that quantify the rates of rotating the triad about  $\mathbf{t}_i^4$ 

$$\frac{d\mathbf{t}_1}{ds} = \omega_2 \mathbf{t}_3 - \omega_3 \mathbf{t}_2$$

$$\frac{d\mathbf{t}_2}{ds} = \omega_3 \mathbf{t}_1 - \omega_1 \mathbf{t}_3$$

$$\frac{d\mathbf{t}_3}{ds} = \omega_1 \mathbf{t}_2 - \omega_2 \mathbf{t}_1$$
(1)

Note that the rates  $\mathrm{d}\mathbf{t}_i/\mathrm{d}s$  are expanded in terms of the vectors orthogonal to  $\mathbf{t}_i$ , which is required by the normalization condition  $\mathbf{t}_i \cdot \mathbf{t}_i = 1$ . Because the contour parameter s has the unit of length, the dimension of velocities  $\omega_i$  is the inverse of length. Only three independent angular velocities  $\omega_i$  are needed, which results from the mutual orthogonality of the triad. The chain conformation is fixed once  $\omega_i(s)$  are known.

Correspondingly, the free energy density along the contour, which measures the costs of bending and twisting, is given at the quadratic order by

$$\beta U(s) = \frac{1}{2} (A_1 \omega_1^2 + A_2 \omega_2^2 + A_3 \omega_3^2)$$
 (2)

Here,  $\beta \equiv 1/(k_{\rm B}T)$ ,  $k_{\rm B}$  is the Boltzmann constant, and T is the temperature. The coefficients  $A_i$  are the elastic moduli for the three rotational modes and, in our convention, have the dimension of length analogous to the persistence length in the WLC model. The model reduces to the standard WLC model by setting  $A_1 = A_2$  and  $A_3 = 0$ . It is useful to relate eq 2 to the kinetic energy of an asymmetric rigid rotor with principal axes  $t_i$  and momenta of inertia  $A_i^{-1}$ , and relate the chain contour to the trajectory of the rigid rotor. Our model is intimately related to the HWLC model considered by Yamakawa. The main difference is that we let the bending moduli be anisotropic and do not consider the effects of intrinsic curvature. However, it should be stressed that the analytical steps presented below are essentially adapted from the treatment of the HWLC model.

**2.1. Green Function of the RLC.** The orientation of a "ribbon" segment,  $\{\mathbf{t}_1, \mathbf{t}_2, \mathbf{t}_3\}$ , can be parametrized using the Euler angles  $\Omega = \{\phi, \theta, \psi\}$  defined in reference to the laboratory frame. In this work, we adopt the ZYZ convention<sup>21</sup> for the Euler angle. As shown in Figure 1c, the azimuthal angle  $\phi$  and polar angle  $\theta$  fix the orientation of  $\mathbf{t}_3$ , around which the twisting angle  $\psi$  is identified, which subsequently fixes the orientations of  $\mathbf{t}_1$  and  $\mathbf{t}_2$ . In Section S.1 in the Supporting Information (SI), the explicit expressions for the Cartesian coefficients of  $\mathbf{t}_i$  are given in terms of  $\Omega$  and, similarly, the angular velocities  $\omega_i$  are expressed in terms of  $\Omega$  as well as  $\dot{\Omega} = \{\dot{\phi}, \dot{\theta}, \dot{\psi}\}$ , where the dot indicates the derivative with respect to s. Therefore, the chain conformations can be parametrized by specifying the variation of the Euler angles along the contour,

i.e.,  $\Omega(s)$ . For the WLC model, the angles  $\phi(s)$  and  $\theta(s)$  are sufficient, whereas for the RLC model, the twisting angle  $\psi(s)$  is also needed.

As far as conformation statistics is concerned, of particular importance is the orientation Green function,  $G(\mathbf{R},\Omega|\Omega_0;L)$ , which measures the probability that the end segment L is positioned at  $\mathbf{R}$  and oriented at  $\Omega$ , given that the starting segment is positioned at the origin and oriented at  $\Omega_0$ . This Green function is the sum of the statistical weights of all legitimate chain conformations and can be expressed via a path integral formulation as  $^4$ 

$$\begin{split} G(\mathbf{R},\,\Omega|\Omega_0;\,L) &= \int_{\Omega(0)=\Omega_0}^{\Omega(L)=\Omega} \mathcal{D}[\Omega(s)] \\ &\delta\bigg(\mathbf{R} - \int_0^L \mathrm{d}s \,\mathbf{t}_3\bigg) \mathrm{exp}\bigg(-\beta \int_0^L \mathrm{d}s U(s)\bigg) \end{split} \tag{3}$$

Here,  $\mathcal{D}[\Omega(s)]$  is a functional integral over the chain conformations or paths whose starting and end orientations are fixed at  $\Omega_0$  and  $\Omega$ . For each such path, the end-to-end separation is calculated from  $\int_0^L \mathrm{d}s\,\mathbf{t}_3$ , which is constrained to the prescribed vector  $\mathbf{R}$  by the  $\delta$ -function. The final exponential is the Boltzmann factor that weights the path by the free energy cost of deformation (eq 2). It is understood that this definition for the Green function will be normalized after an explicit expansion is developed.

Strictly speaking, the results presented in this work do not require end-to-end separation to be constrained. However, introducing the constraint  ${\bf R}$  allows the more general cases to be studied and facilitates the calculation of the higher-order moments of the end-to-end vector. So we present the generic derivation here and specialize to the case of arbitrary  ${\bf R}$  after the governing equation for the Green function is obtained. To proceed, we eliminate the  $\delta$ -function by taking the Fourier transform of eq 3, i.e., applying  $\int d{\bf R} \ {\rm e}^{-{\rm i}{\bf k}\cdot{\bf R}}$  to both sides of eq 3, which gives a characteristic function  $\hat{G}$  depending on the wavevector  ${\bf k}$ ,

$$\hat{G}(\mathbf{k}, \Omega | \Omega_0; L) = \int_{\Omega(0) = \Omega_0}^{\Omega(L) = \Omega} \mathcal{D}[\Omega(s)] \exp \left( i \int_0^L ds \mathcal{L} \right) \tag{4}$$

On the left-hand side, the definition  $\hat{G} \equiv \int d\mathbf{R} \, \mathrm{e}^{-\mathrm{i} \mathbf{k} \cdot \mathbf{R}} \, G(\mathbf{R}, \Omega | \Omega_0; \, L)$  has been substituted. On the right-hand side, the integration factor  $\int d\mathbf{R} \, \mathrm{e}^{-\mathrm{i} \mathbf{k} \cdot \mathbf{R}}$  has been moved inside the path integral, which, when combined with the  $\delta$  function, evaluates to  $\exp(-i\int_0^L d\mathbf{s} \, \mathbf{t}_3)$ . This contribution has been absorbed into the effectively Lagrangian  $\mathcal{L}$  in the last term, in which the imaginary unit "i" connotes the path-integral formulation for the rigid rotor. The effective Lagrangian  $\mathcal{L}$  also contains the deformation free energy and is given by

$$\mathcal{L} = \frac{i}{2} (A_1 \omega_1^2 + A_2 \omega_2^2 + A_3 \omega_3^2) - \mathbf{k} \cdot \mathbf{t}_3$$
 (5)

Although the path integral formulation has a clear physical interpretation, it is more efficient to evaluate the Green function using the "Schrödinger" representation. <sup>4</sup> To do so, we first derive the Hamiltonian using the Legendre transform (Chapter VII, ref 22),  $\mathcal{H} \equiv \sum_{i=1}^{3} p_i \omega_i - \mathcal{L}$ , where  $p_i \equiv \frac{\partial \mathcal{L}}{\partial \omega_i} = A_i \omega_i$  denotes the generalized angular momenta. Substitution of  $\omega_i = p_i/A_i$  gives

$$\mathcal{H} = -\frac{i}{2A_2} (p^2 - \Delta_{12} p_1^2 - \Delta_{23} p_3^2) + \mathbf{k} \cdot \mathbf{t}_3$$
 (6)

in which  $p^2 = p_1^2 + p_2^2 + p_3^2$ ,  $\Delta_{12} = 1 - A_2/A_1$ , and  $\Delta_{23} = 1 - A_2/A_2$  $A_3$ . To find the operator for the angular momenta, we notice that the angular velocity can be written as  $d\omega_i = d\Omega_i/ds$ , where  $\overline{\Omega}_i$  is the accumulated rotation angle around  $\mathbf{t}_i$ . The angles  $\overline{\Omega}_i$ should be differentiated from the Euler angles  $\Omega$ . Although they both specify ribbon orientations,  $\Omega = \{\phi, \theta, \psi\}$  are defined in reference to the laboratory frame, whereas  $\overline{\Omega}_i$  are defined locally, in reference to the ribbon axes t<sub>i</sub>. The relations between the differentials  $d\Omega$  and  $d\Omega_i$  are readily derived from the expressions for  $\omega_{ij}$  as shown in Section S.1. Using these relations, the angular momenta operators  $\mathbf{L}_i \equiv \frac{\mathrm{d}}{\mathrm{d} \bar{\Omega}_i}$  can be expressed as partial derivatives of the Euler angles (Section S.1). Then, substituting  $p_i \rightarrow -i\mathbf{L}_i$  into eq 6 gives the operator form of the Hamiltonian. Note that the operators  $L_i$ should not be confused with the contour variable L (see Chapter 4.1 of ref 23 for the algebraic details of the definition  $L_{ij}$  and Chapter 3.2 of ref 24 for the generalized coordinates).

The Green function therefore satisfies the Schrödinger equation corresponding to the Hamiltonian, eq 6,  $i\frac{\partial \hat{G}}{\partial L} = \mathcal{H}\hat{G}$  with L playing the role of "time". Substituting the operator form of eq 6, nondimensionalizing L as  $N = L/(2A_2)$  and k as  $2A_2k$ , and adopting the convention that  $\hat{G} = 0$  for L < 0, we obtain the Schrödinger equation corresponding to eq 4,

$$\left(\frac{\partial}{\partial N} - \mathcal{A} + i\mathbf{k}\cdot\mathbf{t}_3\right)\hat{G}(\mathbf{k}, \Omega|\Omega_0; L) = \delta(N)\delta(\Omega - \Omega_0)$$
(7)

Here, the inhomogeneous term on the right-hand side ensures that the Green function is properly normalized, and the kinetic energy due to rigid body rotations is given by  $\mathcal{H} \equiv \mathbf{L}^2 - \Delta_{12}\mathbf{L}_1^2 - \Delta_{23}\mathbf{L}_3^2. \text{ Our convention for the Euler angles is such that } \delta\left(\Omega - \Omega_0\right) = \frac{1}{\sin\theta}\delta(\theta-\theta_0)\delta(\phi-\phi_0)\delta(\psi-\psi_0).$ 

The similarity of eq 7 with the quantum mechanical treatment for asymmetric rigid-body rotation is evident. The term  $\mathbf{k} \cdot \mathbf{t}_3$  is reminiscent of the interaction between a dipole and an electric field. Taking the inverse Fourier transform from  $\mathbf{k}$  to  $\mathbf{R}$  gives the equation governing the evolution of  $G(\mathbf{R},\Omega|\Omega_0;N)$ 

where  $\nabla_{\mathbf{R}}$  are the gradient with respect to  $\mathbf{R}$ . When the end-toend separation is not constrained, integrating both sides of the eq 8 for  $\mathbf{R}$  over the whole space gives the free-particle diffusion equation for  $G(\Omega|\Omega_0; N) \equiv \hat{G}(\mathbf{0}, \Omega|\Omega_0; N)$ 

$$\left(\frac{\partial}{\partial N} - \mathcal{A}\right) G(\Omega | \Omega_0; N) = \delta(N) \delta(\Omega - \Omega_0)$$
(9)

which is equivalent to eq 7 with  $\mathbf{k} = 0$ . In the following, we focus on the orientation correlation as revealed by this form of the Green function.

Because the Hamiltonian  $\mathcal{A}$  explicitly depends on all three Euler angles, it is convenient to solve eq 8 by expanding the free-chain Green function using the Wigner  $\mathcal{D}$  functions<sup>21</sup> as the basis set. The Wigner functions  $\mathcal{D}_{mj}^{(l)}$  have three indices that fall into the ranges:  $l \in [0, \infty)$ ,  $m \in [-l, l]$ , and  $j \in [-l, l]$ .<sup>4,21</sup>

The functions  $\mathcal{D}_{mj}^{(l)}$  have several desirable properties: they explicitly depend on the Euler angles, form a complete basis set, and are orthogonal to each other. Moreover,  $\mathcal{D}_{mj}^{(l)}$  are eigenfunctions of  $\mathbf{L}^2$  and  $\mathbf{L}_3$ , and the action of  $\mathbf{L}_1$  and  $\mathbf{L}_2$  only raises or lowers the index j, as shown in Section S.1. Then, the free-chain Green function can be formally expanded as

$$G(\Omega | \Omega_0; N) = \sum_{l=0}^{\infty} \sum_{m=-l}^{l} \sum_{j'=-l}^{l} \sum_{j'=-l}^{l} g_{jj'}^{(l)}(N)$$

$$\mathcal{D}_{mj}^{(l)}(\Omega) \mathcal{D}_{mj'}^{(l)*}(\Omega_0)$$
(10)

Above, only one l index is needed because the functions  $\mathcal{D}_{mj}^{(l)}$  with the same l form an irreducible representation of three-dimensional (3D) rotation. The two  $\mathcal{D}$  functions in the expansion share a common index m because the chain conformation is invariant with respect to whole chain rotation. And the asterisk \* indicates the complex conjugate. Finally, we note that, throughout this work, we distinguish the normalized Wigner function  $\mathcal{D}^{(l)}$  and the standard Wigner function  $\mathcal{D}^{(l)}$ , which are related by  $\mathcal{D}^{(l)} = c_l \mathcal{D}^{(l)}$ , where  $c_l \equiv \left(\frac{2l+1}{8\pi^2}\right)^{1/2}$  are normalization coefficient.

The coefficients  $g_{j'}^{(l)}(N)$  in the Green function can be fixed by substituting eq 10 into eq 9. The right-hand side of eq 9 vanishes for finite N. The properties of the Wigner  $\mathcal{D}$  functions ensure that the Hamiltonian  $\mathcal{A}$  is block-diagonal; each block is labeled by the value of the index l and has dimension  $(2l+1)\times(2l+1)$  (Section S.2). For the block l and when N>0, eq 9 can be written as

$$\frac{\partial}{\partial N} \mathbf{G}^{(l)} = \mathbf{A}^{(l)} \mathbf{G}^{(l)} \tag{11}$$

The entries of  $\mathbf{G}^{(l)}$  are  $g_{jj'}^{(l)}$ , and the entries  $A_{jj'}^{(l)}$  in  $\mathbf{A}^{(l)}$  are evaluated from the overlap integral

$$A_{jj'}^{(l)} = \int \mathrm{d}\Omega \mathcal{D}_{mj'}^{(l)*}(\Omega) \mathcal{H} \mathcal{D}_{mj}^{(l)}(\Omega)$$
(12)

where  $\int d\Omega \equiv \int_0^{\pi} d\theta \sin \theta \int_0^{2\pi} d\psi \int_0^{2\pi} d\psi$ . The explicit expressions to the entries of the symmetric array  $\mathbf{A}^{(l)}$  are given in Section S.2. It is useful to note that the operator  $\mathbf{L}_i$  does not perturb the m indices of the  $\mathcal{D}$ -function, and only modifies the j indices. The entries of the array  $A_{jj}^{(l)}$  are nonzero only when indices j and j' differ by an even number. Since eq 11 is a first-order ODE with constant coefficient, it can be solved using the Laplace transform as detailed in Section S.2. The case of l=0 is trivial:  $g_{00}^{(0)}(L)=1$ . The coefficients for l=1 are especially relevant for our analyses of tangent correlations, so are tabulated in Table 1.

Table 1. Expansion Coefficients  $g_{jj}^{(1)}(L)$  for the Free Particle Green Function<sup>a</sup>

$$\begin{array}{lllll} g_{jj}^{(1)}(L) & j'=-1 & 0 & 1 \\ j=-1 & 1/2(\mathrm{e}^{-L/l_2}+\mathrm{e}^{-L/l_1}) & 0 & 1/2(\mathrm{e}^{-L/l_2}-\mathrm{e}^{-L/l_1}) \\ 0 & 0 & \mathrm{e}^{-L/l_3} & 0 \\ 1 & 1/2(\mathrm{e}^{-L/l_2}-\mathrm{e}^{-L/l_1}) & 0 & 1/2(\mathrm{e}^{-L/l_2}+\mathrm{e}^{-L/l_1}) \end{array}$$

"The relaxation rates or persistence lengths are combinations of stiffness:  $l_1 \equiv 2/(A_2^{-1} + A_3^{-1})$ ,  $l_2 \equiv 2/(A_3^{-1} + A_1^{-1})$ , and  $l_3 \equiv 2/(A_1^{-1} + A_2^{-1})$ .

**2.2. Conformation-Dependent Averages.** Once the Green function, eq 10, is solved, a range of conformational averages, including moments of the end-to-end distance and the radius of gyration, can be readily evaluated. For instance, because the chain end-to-end vector can be calculated from  $\mathbf{R} = \int_0^L \! \mathrm{d}\mathbf{s} \; \mathbf{t}_3$ , the expectation for the squared end-to-end distance  $\langle \mathbf{R}^2 \rangle$  can be written as

$$\langle \mathbf{R}^2 \rangle = 3 \times 2 \int_0^L \mathrm{d}s_2 \int_0^{s_2} \mathrm{d}s_1 \langle t_{3z}(s_2) t_{3z}(s_1) \rangle \tag{13}$$

where  $t_{3z}$  is the z-component of  $\mathbf{t}_3$ . Here and from now on, we use  $\langle \cdot \rangle$  to represent the average over all chain conformations. The factor 3 in eq 13 derives from the application of the relation  $\langle \mathbf{R}^2 \rangle = 3 \langle R_z^2 \rangle$ . The factor 2 accounts for the permutation symmetry, since we constrained the range of  $s_1$  and  $s_2$  such that  $0 \leq s_1 \leq s_2 \leq L$ . The expectation  $\langle t_{3z}(s_2) t_{3z}(s_1) \rangle$  is an average over all valid chain conformations, regardless of the orientations of, in particular, the end segments  $\Omega_0$  and  $\Omega_L$ . Using the Markov property of the Green function, we have

$$\begin{split} \langle t_{3z}(s_2)t_{3z}(s_1)\rangle \\ &= \int \mathrm{d}\Omega_L \int \mathrm{d}\Omega_2 \int \mathrm{d}\Omega_1 \int \mathrm{d}\Omega_0 t_{3z}(\Omega_2)t_{3z}(\Omega_1) \cdot \\ &G(\Omega_L | \Omega_2; \ L - s_2)G(\Omega_2 | \Omega_1; \ s_2 - s_1)G(\Omega_1 | \Omega_0; \ s_1) \end{split} \tag{14}$$

Because the tangents  $t_{3z}$  depend on segmental index s via the Euler angles  $\Omega$ , we have explicitly written  $t_{3z}(\Omega_2)$  and  $t_{3z}(\Omega_1)$ . Similar conventions are adopted below.

Each of the three Green functions in eq 14 can be expanded in terms of the Wigner  $\mathcal{D}$  functions using eq 10. The variation of indices of the  $\mathcal{D}$  functions along the chain contour is labeled in Figure 2. For instance, between segments 0 and  $s_1$ , the

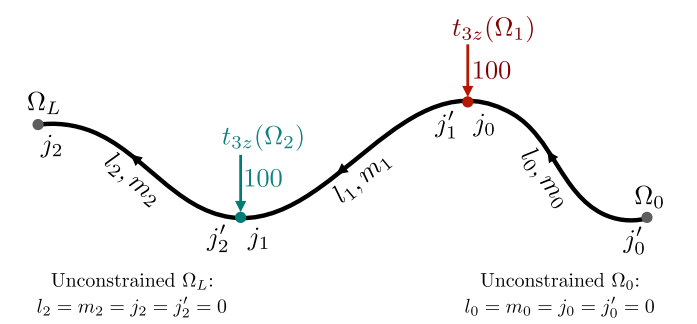


**Figure 2.** Convention for the indices in Wigner  $\mathcal{D}$  functions used in the calculation of  $\langle R_z^2 \rangle$ . Indices  $l_i$  and  $m_i$  (i=0,1,2) remain constant for  $0 < s < s_1, s_1 < s < s_2$ , and  $s_2 < s < L$ , respectively. Pairs of indices  $j_i$  and  $j_i'$  are needed by the coefficients  $g_{jj_i'}^{(l_i)}$ , which is nonzero when  $|j_i-j_i'|$  is even. Three such coefficients are needed because two internal segments  $s_1$  and  $s_2$  are included. Tangent components  $t_{3z}$  raise or lower indices  $l_i$ .

Green function  $G(\Omega_1|\Omega_0; s_1)$  is parametrized by indices  $l_0, m_0, j_0$ , and  $j'_0$ , and equals the sum of the products,  $g^{(l_0)}_{j_0j'_0}(s_1)\mathcal{D}^{(l_0)}_{m_0j_0}(\Omega_1)\mathcal{D}^{(l_0)^*}_{m_0j'_0}(\Omega_0)$ . The other two Green functions,  $G(\Omega_2|\Omega_1; s_2-s_1)$  and  $G(\Omega_L|\Omega_2; L-s_2)$ , are expanded by using the corresponding indices shown in Figure 2. The summation can be greatly simplified using the symmetry and the orthogonality relations of the  $\mathcal D$  functions.

For example, the unconstrained orientations of the two end segments restrict the range of indices of  $\mathcal{D}$  functions. The integral  $\int d\Omega_0 \mathcal{D}_{m_0j_0'}^{(l_0)}(\Omega_0)$  is nonzero only for the isotropic  $\mathcal{D}$  function, i.e.,  $l_0 = m_0 = j_0' = 0$  and, consequently,  $j_0 = 0$ . By analogy, the integral over  $\Omega_L$  requires  $l_2 = m_2 = j_2 = j_2' = 0$ . These simplifications reduce eq 14 to

$$\int d\Omega_{2} \int d\Omega_{1} \mathcal{D}_{00}^{(0)}(\Omega_{2}) t_{3z}(\Omega_{2}) G(\Omega_{2} | \Omega_{1}; s_{2} - s_{1}) t_{3z}(\Omega_{1})$$

$$\mathcal{D}_{00}^{(0)}(\Omega_{1}) \tag{15}$$

In Section S.3, we demonstrate that the tangent components,  $t_{3z}(\Omega_1)$  and  $t_{3z}(\Omega_2)$ , as well as all other components of the vectors  $\mathbf{t}_i$ , can be expanded using the linear combinations of functions  $\mathcal{D}_{mj}^{(l)}$  with l=1. Then, the conformation averages are reduced to the integrals of the products of the Wigner  $\mathcal{D}$  functions. The orthogonality relations of  $\mathcal{D}$  functions allow us to identify selection rules for the surviving indices, e.g.,  $l_1$ ,  $m_1$ ,  $j_1$ , and  $j_1'$  in Figure 2. These details are explained in Section S.4, which shows specifically that

$$\langle t_{3z}(s_2)t_{3z}(s_1)\rangle = \frac{1}{3}g_{00}^{(1)}(s_2 - s_1)$$
 (16)

Evaluating higher moments involving, e.g.,  $\mathbb{R}^4$ , requires the nested expansion of the Green functions and vectors  $\mathbf{t}$ . The resulting cumbersome algebra can be greatly simplified by using the "stone-fence" diagrams, <sup>4,25</sup> which diagrammatically track the selection rules, i.e., the variation of the indices of the  $\mathcal{D}$  functions along the chain contour, that contribute nontrivially to the conformation averages. The detailed algebraic steps and explicit examples for constructing stone-fence diagrams are provided in Section S.5.

# 3. RESULTS

A variety of conformational properties of RLCs are obtained after the Green function is solved. The general idea is discussed in Section 2.2 and is detailed in Sections S.3 and S.4. We first examine the orientation correlation along the chain and then provide expressions for the end-to-end distance squared and radius of gyration. The last two parts focus on the shape of ribbon-like oligomers. In all cases, the effects of the bending and twisting moduli are of focus. When relevant, the effects of molecular weights and crossover to the WLC limit are discussed.

**3.1. Orientation Correlations.** The unique feature regarding chain conformation captured by the RLC model, compared to the WLC model, is the transverse orientation of the chain segments. The correlation functions of the normal, binormal, and tangent vectors, respectively, reveal the effects of anisotropic bending stiffness. Section S.4 shows that all of the diagonal (eq S.20) and cross-correlations (eqs S.21 and S.22) of the three vectors  $\mathbf{t}_1$ ,  $\mathbf{t}_2$ , and  $\mathbf{t}_3$  can be expressed using the entries  $g_{jj}^{(1)}$ . Although we focus on the RLC model in this work, it is useful to note that these expressions are not restricted by the choice of model Hamiltonian. For instance, the same expressions can be used for analyzing the orientational correlation of the helical worm-like chains, or of the model that incorporates the bending-twist coupling.

For the RLC model, by substituting the symmetry of Table 1, we find that the three cross-correlations  $\langle \mathbf{t}_i(L) \cdot \mathbf{t}_j(0) \rangle$   $(i \neq j)$  all vanish, similar to the WLC model, while the autocorrelation functions can be written

$$\langle \mathbf{t}_{1}(L) \cdot \mathbf{t}_{1}(0) \rangle = g_{11}^{(1)}(L) - g_{1\overline{1}}^{(1)}(L)$$
 (17)

$$\langle \mathbf{t}_{2}(L) \cdot \mathbf{t}_{2}(0) \rangle = g_{11}^{(1)}(L) + g_{1\bar{1}}^{(1)}(L)$$
(18)

$$\langle \mathbf{t}_3(L) \cdot \mathbf{t}_3(0) \rangle = g_{00}^{(1)}(L) \tag{19}$$

The last line is seen to be consistent with eq 16 because the conformation statistics of free chains is isotropic. Further expansion yields

$$\langle \mathbf{t}_i(L) \cdot \mathbf{t}_i(0) \rangle = e^{-L/l_i} \quad (i = 1, 2, 3)$$

where the decay rates  $l_i$  are determined by the bending or twisting moduli, as defined in the caption of Table 1, which may be concisely written as  $l_i \equiv \frac{2}{A_i^{-1} + A_k^{-1}}$ , where  $j \neq i$ ,  $k \neq i$ ,

and  $j \neq k$ . These expressions are expected based on the symmetry of the Hamiltonian. The tangent  $\mathbf{t}_3$ , for example, is decorrelated not by self-rotation or twist, which is governed by  $A_3$ , but by rotations about  $\mathbf{t}_1$  and  $\mathbf{t}_2$ , which are governed by  $A_1$  and  $A_2$ , respectively. The absence of coupling among  $\omega_1$ ,  $\omega_2$ , and  $\omega_3$  in eq 6 ultimately leads to the independent relaxations of the normal, binormal, and tangent vectors. Eq 20 shows that locally, the polymer may primarily "undulate" (rotate about  $\mathbf{t}_2$ ), "twist" (rotate about  $\mathbf{t}_3$ ), or "turn" in-plane (rotate about  $\mathbf{t}_1$ ) depending on the relative values of  $A_1$ ,  $A_2$ , and  $A_3$  (Figure 1). In particular, the twist mode is effective in decorrelating the orientations of  $\mathbf{t}_1$  and  $\mathbf{t}_2$ .

Equation 20 generalizes the result of the tangent vector,  $\langle \mathbf{t}_3(L) \cdot \mathbf{t}_3(0) \rangle = \mathrm{e}^{-L/l_\mathrm{p}}$ , for the WLCs, in which  $l_\mathrm{p}$  is the standard persistence length. By analogy, we introduced three persistence lengths  $l_i$ . Setting  $A_1 = A_2$  and  $A_3 = 0$  in eqs 20 recovers the WLC behavior. The normal  $\mathbf{t}_1$  and binormal  $\mathbf{t}_2$  decorrelate instantly because the twist is not penalized and the WLC cannot differentiate  $t_1$  and  $t_2$ . Equation 20 becomes  $\langle \mathbf{t}_3(L) \cdot \mathbf{t}_3(0) \rangle = \mathrm{e}^{-L/l_3}$  for the tangent correlation, with  $l_3 = A_1 = A_2$ , which reduces to  $l_\mathrm{p}$  in the WLC model. On the other hand, setting  $A_1 \to \infty$  and  $A_2 \to \infty$  gives the rod-like behavior: the tangent vector does not relax.

The rates of exponential decay in eqs 20 are consistent with the short time behavior of the Green function. In the "short time" limit, by setting  $L \to 0$ , it can be shown that eq 9 in the domain L > 0 reduces to a diffusion equation with anisotropic diffusivities

$$\frac{\partial G}{\partial L} = \frac{1}{2} \left( \frac{1}{A_1} \frac{\partial^2}{\partial \theta_1^2} + \frac{1}{A_2} \frac{\partial^2}{\partial \theta_2^2} + \frac{1}{A_3} \frac{\partial^2}{\partial \psi^2} \right) G \tag{21}$$

Because the orientation of the starting point  $\Omega_0$  is irrelevant, to obtain the above limit, we have set  $\theta_0 = \pi/2$  for convenience. This choice decouples the contributions from the twist mode and the two bending modes. The partials  $\partial/\partial\theta_1$  and  $\partial/\partial\theta_2$  give the variations due to bending along the  $\mathbf{t}_1$  and  $\mathbf{t}_2$  axes, respectively, and the partial  $\partial/\partial\psi$  gives that due to twist along the ribbon tangent  $\mathbf{t}_3$ .

The fluctuations of the three angles follow the prediction of the anisotropic diffusion equation (eq 21) and are expressed using the "diffusivity"  $1/A_i$ :  $^{26}\langle(\delta\theta_1)^2\rangle=L/A_1$ ,  $\langle(\delta\theta_2)^2\rangle=L/A_2$ , and  $\langle(\delta\psi)^2\rangle=L/A_3$ . These fluctuations can be related to the correlation functions in eq 20. For instance, the variation in the tangent vector results from bending modes. The contribution from small  $\theta_1$  gives  $\mathbf{t}_3(L)\cdot\mathbf{t}_3(0)=\cos\theta_1\simeq 1-\theta_1^2/2$ . The contribution from  $\theta_2$  is analogous. Combining the two contributions gives

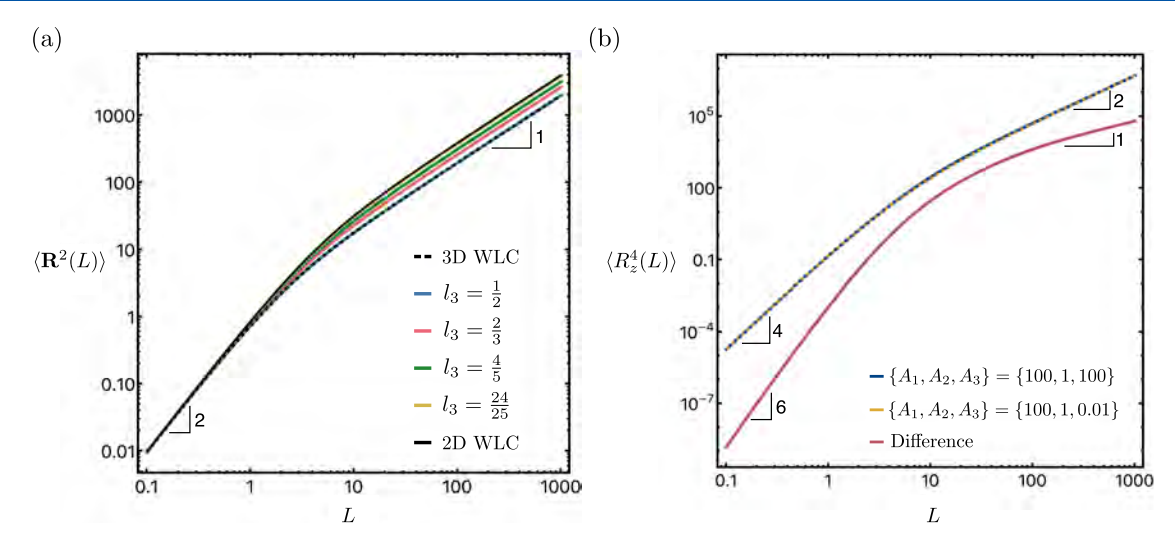


Figure 3. Variation of chain size with molecular weight. (a)  $\langle \mathbf{R}^2(L) \rangle$  for the RLC and WLC with various stiffness parameters. (b) Effect of twisting stiffness  $(A_3)$  on  $\langle R_2^4(L) \rangle$ ; "difference" is the orange trace subtracted from the blue one.

$$\begin{split} \langle \mathbf{t}_3(L) \cdot \mathbf{t}_3(0) \rangle &\simeq 1 - \frac{1}{2} \langle \theta_1^2 \rangle - \frac{1}{2} \langle \theta_2^2 \rangle \\ &= 1 - \frac{L}{2} \left( \frac{1}{A_1} + \frac{1}{A_2} \right) \end{split} \tag{22}$$

which agrees with the short-time behavior of eq 20 for i = 3. Similar asymptotic results can be obtained to match the cases i = 1, 2. However, it is important to note that eqs 20 is exact for the full range of L values.

**3.2. Chain Size.** Below we present results for the end-to-end distance squared and the radius of gyration, calculated using the stone-fence diagram. It suffices to consider the moments the z-component for the end-to-end vector (nonzero for even n)

$$\langle R_z^n \rangle = n! \int_0^L ds_n \int_0^{s_n} ds_{n-1} \\ \cdots \int_0^{s_2} ds_1 \langle t_{3z}(s_n) t_{3z}(s_{n-1} \cdots t_{3z}(s_1) \rangle$$
 (23)

The average  $\langle \cdot \rangle$  is over all possible chain conformations and segmental orientations. The factorial 'n!' accounts for the multiplicity of "time-ordering",  $s_1 < s_2 < \cdots < s_n$ . The n-point correlation for ordered segments can be written as products of 2-point correlations using the Markov property of conformation statistics, which includes  $G(\Omega_1|\Omega_0; s_1)$ ,  $G(\Omega_2|\Omega_1; s_2 - s_1)$ ,  $\cdots$   $G(\Omega_L|\Omega_n; L - s_n)$ . Eq 10 can then be substituted for all of the two-point correlation functions. Finally, an average is performed over the orientations of both internal and end segments. For n=1,  $\langle R_x^2 \rangle = \langle R_y^2 \rangle = \langle R_z^2 \rangle = \langle R^2 \rangle/3$  because the integrals over  $\Omega_0$  and  $\Omega_L$  in eq 23 are isotropic.

Substituting eq 16 into eq 23, while keeping the factor 3, gives

$$\langle \mathbf{R}^2(L) \rangle = L^2 g_D(L/l_3) \tag{24}$$

The dependence on contour length is contained in the Debye function,  $g_D(x) \equiv \frac{2}{x^2}(x-1+e^{-x})$ , which approaches 1-x/3 as  $x \to 0$ , and approaches 2/x as  $x \to \infty$ .

This result is formally identical to that of the WLC. Both types of chains are rod-like at short chain length. Their differences are notable in the crossover regime. For the RLC,

as L increases, chains may decorrelate from their initial direction by rotating around either  $\mathbf{t}_1$  or  $\mathbf{t}_2$ , which are identical in the WLC. Therefore, RLCs with  $A_1 = A_2$  have  $\langle \mathbf{R}^2 \rangle$  identical to the WLC. However, RLCs with disparate bending stiffness,  $A_1 \gg A_2$  (or vice versa), have only one relaxation mode, effectively doubling  $l_3$ . Because the stiffer mode is quenched, the RLC behaves like a 2D WLC in this limit (Figure 3a, solid black line), exhibiting an extended rod-like regime compared to the 3D WLC. Eventually, all chains progress to the coil-like regime, where  $\langle \mathbf{R}^2 \rangle \sim L$  (Figure 3a).

The twisting stiffness  $A_3$  is absent in eq 24 because the twisting mode is decoupled from the two bending modes in eq 6. Thus, twisting about  $\mathbf{t}_3$  does not deflect the chain (does not alter  $\mathbf{t}_3$ ), and therefore does not affect  $\langle \mathbf{R}^2(L) \rangle$ . The twisting stiffness does contribute to higher-order moments of  $\langle \mathbf{R}^n \rangle$ , through their appearance in coefficients  $g_{00}^{(l)}(L)$  for  $l \geq 2$ , but the effect is modest. In the case of  $\langle R_z^4 \rangle$ , the chain stiffness is most significantly enhanced during the rod-to-coil transition (up to about 15%, Figure 3b) by increasing the twisting stiffness. Though the twisting stiffness does not materially alter the end-to-end moments of the chain, it significantly affects the segmental orientations. These results are discussed in the next section.

The squared radius of gyration is calculated as

$$\langle R_g^2(L) \rangle = \frac{1}{L^2} \int_0^L ds_2 \int_0^{s_2} ds_1 \langle \mathbf{R}^2(s_2 - s_1) \rangle$$
 (25)

Substituting eq 24 into the above yields

$$\langle R_{\rm g}^2(L) \rangle = l_3^2 \left( \frac{L}{3l_3} - 1 + g_{\rm D}(L/l_3) \right)$$
 (26)

The result in the WLC limit agrees exactly with  $\langle R_{\rm g}^{\ 2}(L) \rangle$  for the WLC. As such, its interpretation parallels that of eq 24. The literature has reported the use of the WLC expression for estimating the persistence length. Our result suggests that this persistence length needs to be interpreted with caution, as it does not contain contributions from the twisting mode and it depends on the average of two orthogonal bending modes.

**3.3. Chain Shape: Molecular Weight Effect.** We showed in the preceding section that twist stiffness  $A_3$  does not contribute to  $\langle \mathbf{R}^2 \rangle$  nor  $\langle R_{\mathbf{g}}^2 \rangle$  in the RLC model. This section

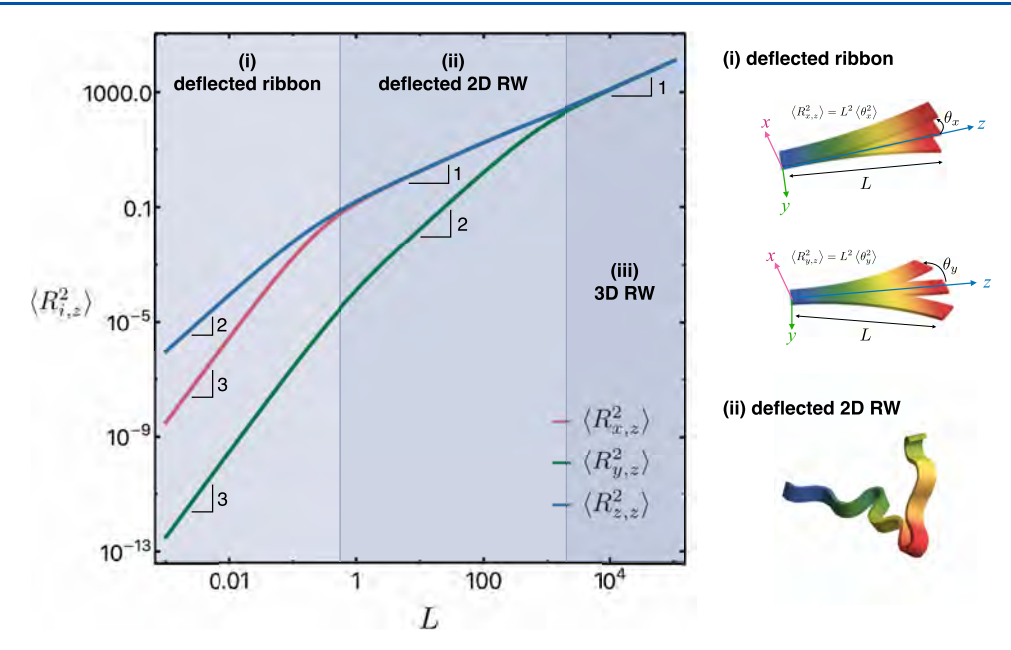


**Figure 4.** Expectation values of x, y, and z components for the end-to-end vector of a ribbon with fixed initial orientation. Three distinct scaling regimes of molecular weight dependence are identified for the chosen parameters,  $A_1 = A_3 = 10^3$  and  $A_2 = 0.1$ : (i) deflected ribbon, (ii) deflected 2D RW (random walk), and (iii) 3D RW. The representative chain conformations in the first two regimes are schematically shown.

discusses the influence of  $A_3$  on chain shape by examining the moments of the end-to-end vector for a chain initially aligned in the z-direction (Figure 4)

$$\langle R_{i,z}^2 \rangle = \int_0^L ds_1 \int_0^L ds_2 \langle t_{3i}(s_2) t_{3i}(s_1) \rangle, \ i \in \{x, y, z\}$$
(27)

The averages evaluated here differ from the previous section in that the orientation of one end segment, say,  $\Omega_0$ , is anchored. The subscript "z" indicates that the tangent  $\mathbf{t}_3$  of the initial ribbon is oriented along the z axis. Such a constrained average allows for direct visualization of the effects of twisting on both local and long-ranged conformational statistics and is useful for examining the conformation of chains near the interface between crystalline and amorphous domains. The procedure adopted for evaluating eq 27 is analogous to the previous section, and the stone-fence diagrams contributing to the average are shown in Figure S.3 (SI).

The variation of the expectations  $\langle R_{i,z}^2 \rangle$  with the contour length L is shown in Figure 4, for parameters  $A_2=0.1$  and  $A_1=A_3=10^3$ . This choice gives similar behavior as that considered by Nyrkova et al. (The general case will be discussed in the next section.) Because  $A_1$  and  $A_3$  are comparatively large, rotation about  $\mathbf{t}_2$  is the active relaxation mode at a short L. Depending on how the contour length compares to the persistence lengths,  $l_1=l_3\simeq A_2/2$  and  $l_2=A_1\gg l_1$ , three distinct scaling regimes are observed, which are labeled in Figure 4 as (i) deflected ribbon, (ii) deflected 2D RW (random walk), and (iii) 3D RW.

Regime (i):  $L < l_3$ . The contour length is below the smallest persistence length, and the ribbon has a prescribed orientation along the z-axis. Therefore,  $R_{z,z}$  behaves as that of a rigid rod with length L, and  $\langle R_{z,z}^2 \rangle \simeq L^2$ . On the other hand, finite bends or deflections are possible within the x-z plane, which lead to nonvanishing contributions to  $\langle R_{x,z}^2 \rangle$ . For the small deflection angle  $\theta_x$  (Figure 4),  $R_{x,z}(L) = L\theta_x$ . Thus, the value is  $\langle R_{x,z}^2(L) \rangle = \langle (L\theta_x)^2 \rangle = L^2 \langle \theta_x^2 \rangle$ . The changing rate of tangent vector, over an arc of length L due to the deflection by a small angle is  $\theta_x/L$ .

The corresponding bending energy is  $l_3$  ( $\theta_x/L$ ) $^2$  L/2, which leads to the expectation  $\langle \theta_x^2 \rangle = L/l_3$ . Therefore, we expect  $\langle R_{x,z}^2(L) \rangle = L^3/l_3$ . The in-plane bend, by an angle  $\theta_y$  (Figure 4), is much harder and is controlled by the persistence length  $l_2$ . Similar analysis leads to  $\langle \theta_y^2 \rangle = L/l_2$  and  $\langle R_{y,z}^2 \rangle = L^3/l_2$ . Figure 4 confirms these scalings with respect to the molecular weight.

Regime (ii):  $l_3 < L < l_2$ . Although the in-plane bending mode and the twist mode are still quenched, the out-of-plane bending is fully activated. The chain conformations are mostly confined within the x-z plane, analogous to that of a 2D random walk. Therefore, the expectation values for  $\langle R_{z,z}^2 \rangle$  and  $\langle R_{x,z}^2 \rangle$  both equal to  $Ll_3$ , half that of the end-to-end distance squared for a 2D random walk  $\langle R_{\parallel}^2 \rangle$ . Although the 2D random walk is the average conformation adopted by the chain contour, the out-of-plane deflection caused by a small twist along the z axis or bending along the x axis is possible. The average deflection angle is  $\langle \theta^2 \rangle = 2L/A_1 = 2L/A_3$ , or  $\langle \theta^2 \rangle \simeq L/l_2$ . The product of contribution from the deflection angle and the span of 2D random walk gives  $\langle R_{y,z}^2 \rangle \simeq \langle R_{\parallel}^2 \rangle \langle \theta^2 \rangle = L^2 l_3/l_2$ . The characteristic scaling exponents are labeled in Figure 4.

Regime (iii):  $l_2 < L$ . The chain adopts 3D random walk conformations. The average chain end-to-end distance is given by  $2Ll_3$ , which is split evenly among the three components. We therefore expect  $\langle R_{x,z}^2 \rangle = \langle R_{y,z}^2 \rangle = \langle R_{z,z}^2 \rangle = 2Ll_3/3$ . The exponent for L-dependence is shown in Figure 4.

The above results are summarized in Table 2, in which the nonessential numerical prefactors are dropped. It is straightfor-

Table 2. Scaling Regimes for the Components of the Endto-End Vector Squared, for  $A_2 \ll A_1 = A_3^a$ 

	$L < l_3$	$l_3 < L < l_2$	$l_2 < L$
$\langle R_{x,z}^2 \rangle$	$L^3/l_3$	$L l_3$	$L l_3$
$\langle R_{y,z}^2 \rangle$	$L^{3}/l_{2}$	$L^2 l_3/l_2$	$L l_3$
$\langle R_{z,z}^2 \rangle$	$L^2$	$L l_3$	$L l_3$

<sup>a</sup>One end of the ribbon is anchored, and another end initially points along the z axis. Note that  $l_1 = l_3$  in this specific case.

ward to verify that the expressions in different regimes cross over smoothly at  $L = l_3$  and  $L = l_2$ , for all three components.

**3.4. Chain Shape: Stiffness Effect.** The scaling regimes and crossovers discussed in the previous section form the basis to understanding the effects of arbitrary combinations of stiffness. The RLC model contains three parameters,  $A_1$ ,  $A_2$ , and  $A_3$ . Without loss of generality, we choose the *smaller* bending modulus as a common reference and denote it, for concreteness, as  $A_2$ , which defines the length unit and can be treated as fixed. Therefore, the RLC is uniquely specified by two ratios: the anisotropy parameter  $A_1/A_2$  ( $A_1/A_2 \ge 1$ ) and the twist parameter  $A_3/A_2$  ( $A_3/A_2 \ge 0$ ). The values of these ratios are both large for the case discussed in Section 3.3.

More generally, we may map the conformational properties of the RLCs to the diagram sketched in Figure 5, in which the

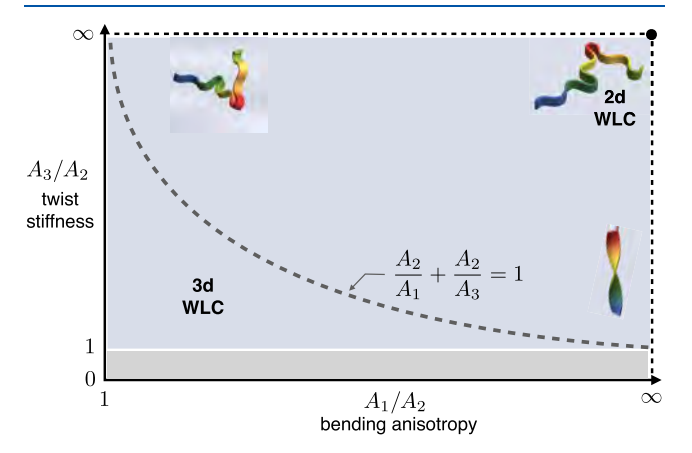


**Figure 5.** Effects of stiffness on segmental shape. The variation of segmental shape due to either twisting or the secondary bending is shown schematically, near the edges of softened twist stiffness or bending anisotropy.

x-axis measures the degree of anisotropy and the y-axis measures the twist stiffness. The top-right corner of this diagram represents the 2D WLC since, with one finite bending modulus  $A_2$ , the chain is strictly confined to a plane.

3D WLC statistics are reached in two different limits. The first is the left edge of the diagram with  $A_1 = A_2$ . In this limit, as far as the tangent orientation is concerned, the conformational statistics are identical to those for the 3D WLC. The second is the bottom edge of the diagram, with  $A_3 \rightarrow 0$ . Because the

twists are not penalized, by the time any bending mode is activated, the ribbon has been twisted multiple times, having an effectively isotropic stiffness and a persistence length  $l_3$ .

Along the right edge, the 2D WLC behavior evolves smoothly to that of 3D WLC as the  $A_3$  decreases. For finite  $A_3$  values, the expectations  $\langle R_{i,z}^2 \rangle$  for i=x,y, and z follow the L dependence summarized in Table 2. The chain conformations go through regimes i–iii as  $A_3$  is decreased. Specifically, the crossover between regimes (i) and (ii) occurs when the twist mode is activated. The anticipated scaling forms are confirmed by the ratios  $\langle R_{x,z}^2 \rangle / \langle R_{y,z}^2 \rangle$  and  $\langle R_{z,z}^2 \rangle / \langle R_{x,z}^2 \rangle$  plotted in Figure 6a,b. The ratio  $\langle R_{x,z}^2 \rangle / \langle R_{y,z}^2 \rangle$  plateaus for small L, decays according to  $L^{-1}$  for  $L > l_3$ , and then plateaus to unity in the 3D random walk regime for  $L > l_2$ . The width of the second regime widens with increasing  $A_3$ , and the plateau value in the small L regime reaches a constant  $A_1/A_2$  for a sufficiently large  $A_3$ . On the other hand, the ratio  $\langle R_{z,z}^2 \rangle / \langle R_{x,z}^2 \rangle$  decays as  $L^{-1}$  in the small L regime, and approaches unity for  $L > l_3$ .

The behavior along the top edge is entirely analogous. As  $A_1$  is reduced, the 2D WLC behavior evolves to that of the 3D WLC, only now the randomization leading to the 3D random walk behavior is caused by the bending mode governed by  $A_1$ .

The L dependence is similar when  $A_1/A_2$  and  $A_3/A_2$  are both finite and the randomizing modes include contributions from both twisting and bending. Figure 6c illustrates the effects of varying  $A_2$  while  $A_3$  and  $A_1$  are fixed. The dashed line in Figure 5 that separates 2D WLC and 3D WLC behavior is an estimate given by  $1/A_1 + 1/A_3 = 1/A_2$ . Furthermore, the shapes of the chain segment due to the softened twist or bending stiffness are also sketched in Figure 5. It is important to notice that the condition for 3D random walk behavior is  $L > l_2$ , instead of the condition  $L > l_3$  for the 3D WLC.

## 4. CONCLUSIONS

The RLC model explored here extends the WLC model to capture anisotropic bending stiffnesses evident in the CP and ladder polymer conformations. We calculate the free-chain Green function, which is a key quantity for investigating RLC statistics. Predictions of end-to-end moments and chain shape highlight the influence of bending anisotropy and twisting stiffness on RLC conformational statistics, laying the foundation for a more detailed characterization of structure—function relationships in the design of CPs and ladder polymers. The RLC tangent—tangent correlation functions give essentially the same information as that for the WLC

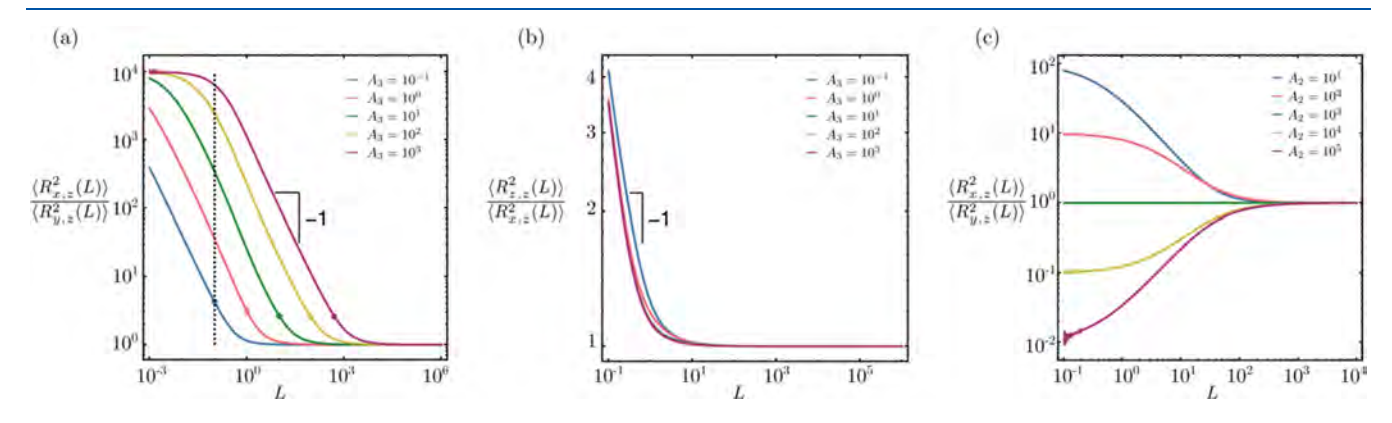


**Figure 6.** Contour length dependence for ribbon shape. (a) Ratio of the x- and y-components of the end-to-end distance squared for  $A_2 = 0.1$ ,  $A_1 = 10^3$ , and varying  $A_3$ . (b) Same as (a) but for the ratio of the z- and x-components. (c) Ratio of the x- and y-components of the end-to-end distance squared for  $A_1 = 10^3$ ,  $A_3 = 10$ , and varying  $A_2$ .

model, as long as the persistence length is interpreted as the harmonic average of the two bending stiffnesses. However, in contrast to the WLC model, the RLC correlation functions of the normal and the binormal vectors provide information on the conjugation length along CP backbones, which connects to the conductivity. The twisting stiffness plays a crucial role in determining such correlations. Overall, the conformation statistics of the RLC is determined by the ratios  $A_1/A_2$  (bending anisotropy) and  $A_3/A_2$  (twisting stiffness), as summarized in Figure 5 and Table 2.

A natural application for RLC is investigating the influence of polymer chemistry on the bending and twist stiffness. Both CPs and ladder polymers can be studied, and we choose CPs as the example to facilitate the discussion, which are often oligomeric. All-atom molecular dynamics (MD) simulation provides complete structural information for a classical approximation of CP films, including the position and orientation of the polymer backbone. By imposing the axes  $t_i$ on each monomer throughout the simulation, the bending stiffnesses  $\{A_i\} = \{A_1, A_2, A_3\}$  extracted from an optimized fit of eq 20 sampled in MD. Comparing  $\{A_i\}$  between polymers will show the influence of polymer chemistry on conformational behavior. For example, the effects of side chains, singlevs double-stranded backbones, or aromatic vs aliphatic backbones may be investigated. The effect of film processing on CP microstructure may be more robustly investigated as well provided accurate and affordable simulation protocols are available. These calculations will illuminate structure-function relationships for engineering CP flexibility while also providing insight into the applicability of the RLC model.

Comparing the parameters derived from simulation to those derived from experiments is an important task. Because there are three distinct bending stiffnesses in the RLC, three distinct experimental measurements would be required to unambiguously parametrize the chain. One such measurement is small-q light scattering, where the squared radius of gyration may be calculated from the form factor, P(q), in the Guinier regime<sup>27</sup>

$$P(q) = \exp\left(-\frac{q^2 R_{\rm g}^2}{3}\right) \tag{28}$$

By means of eq 25, this measurement would determine  $l_3$ . Two other measurements are needed that provide  $l_1$  and  $l_2$ , or an appropriate combination of  $\{A_i\}$ . For example, Förster resonance energy transfer (FRET) spectra are dependent on both the distance and relative orientation of the donor and acceptor and therefore may give insight into the free-chain Green function,  $G(\Omega \mid \Omega_0; L)$ .

Field-theoretic calculations are a natural complement to experimental and computational investigations of the RLC film microstructure. It has been shown that, under the influence of a nematic director, WLC films may assemble in isotropic or nematic phases depending on the material parameters. Given that the RLC has anisotropic bending and that  $\pi$ - $\pi$  stacking in CP films is a directional interaction, it is expected that RLC films may break uniaxial symmetry under certain conditions, leading to domains where biaxial ordering is dominant. Developing a mean-field theory for the RLC incorporating these interactions represents an important step toward a better understanding of CP film morphology. Using the stiffness parameters benchmarked from atomistic simulations, the field theory may be extended to study specific systems in more detail, such as the inclusion of surface effects or confinement,

backbone charge for polyelectrolytes, <sup>29</sup> length asymmetry in chains for polymer—polymer or small molecule—polymer blends, <sup>30</sup> and fluctuation corrections when chain conformations or precise phase boundaries are important.

An intriguing feature neglected in this work is the twist-bend coupling. In the RLC, we envision twisting about the CP backbone purely as a rotation about  $t_3$ . However, in CPs, intermediate dihedral angles between the cis and trans configurations also perturb t<sub>3</sub> relative to the planar configurations. Thus, the geometry of CPs creates inherent twist-bend coupling. It remains to be tested whether eq 20 captures the conformation properties of CPs with proper choices of  $\{A_i\}$ . Recent simulations have observed persistent oscillation in the tangent-tangent correlations.<sup>6</sup> We will present ongoing work elsewhere that analyzes such effects by including the twist-bending coupling into eq 6. Finally, we stress that the RLC model evolves to the Gaussian-chain behavior in the long-chain limit. The model is particularly useful when the functional properties of oligomeric polymers are sensitive to the conformation features at the intermediate scale.

#### ASSOCIATED CONTENT

## **Solution** Supporting Information

The Supporting Information is available free of charge at https://pubs.acs.org/doi/10.1021/acs.macromol.3c01430.

Parametrization of ribbon orientation and angular momentum operator (S.1), calculation of expansion coefficients for the Green function (S.2), expansion of orientation vectors using the Wigner function (S.3), algebraic details for calculations of the orientation correlations (S.4), and index convention for the stone-fence diagrams (S.5) (PDF)

## AUTHOR INFORMATION

#### **Corresponding Authors**

Wesley Michaels — Department of Chemical Engineering, Stanford University, Stanford, California 94305, United States; Email: wpm216@stanford.edu

Jian Qin — Department of Chemical Engineering, Stanford University, Stanford, California 94305, United States; orcid.org/0000-0001-6271-068X; Email: jianq@stanford.edu

#### Author

Andrew J. Spakowitz — Department of Chemical Engineering, Stanford University, Stanford, California 94305, United States; Department of Materials Science and Engineering, Department of Applied Physics, and Department of Chemistry, Stanford University, Stanford, California 94305, United States; Occid.org/0000-0002-0585-1942

Complete contact information is available at: https://pubs.acs.org/10.1021/acs.macromol.3c01430

#### Notes

The authors declare no competing financial interest.

#### ACKNOWLEDGMENTS

W.M. acknowledges funding from the David G. Mason Fellowship from the Stanford University Department of Chemical Engineering. W.M. gratefully acknowledges funding from the National Science Foundation Graduate Research

Fellowship Program (grant no. DGE 1656518). W.M. and J.Q. acknowledge seed grant support from the Precourt Institute for Energy at Stanford University. A.J.S. was supported by the NSF program Condensed Matter and Materials Theory (DMR-1855334). W.M. and J.Q. thank helpful conversations with Srikant Sagireddy and Sheng-Lun (Mark) Liao.

## REFERENCES

- (1) Kratky, O.; Porod, G. Röntgenuntersuchung gelöster Fadenmoleküle. Recl. Trav. Chim. Pays-Bas 1949, 68, 1106–1122.
- (2) Spakowitz, A. J. Wormlike chain statistics with twist and fixed ends. *Europhys. Lett.* **2006**, 73, 684. Publisher: IOP Publishing.
- (3) Obermayer, B.; Frey, E. Tension dynamics and viscoelasticity of extensible wormlike chains. *Phys. Rev. E* **2009**, *80*, No. 040801. Publisher: American Physical Society.
- (4) Yamakawa, E. H. Helical Wormlike Chains in Polymer Solutions; Yamakawa, E. H., Ed.; Springer: Berlin, Heidelberg, 1997.
- (5) Giomi, L.; Mahadevan, L. Statistical Mechanics of Developable Ribbons. *Phys. Rev. Lett.* **2010**, *104*, No. 238104. Publisher: American Physical Society.
- (6) Root, S. E.; Jackson, N. E.; Savagatrup, S.; Arya, G.; Lipomi, D. J. Modelling the morphology and thermomechanical behaviour of low-bandgap conjugated polymers and bulk heterojunction films. *Energy Environ. Sci.* **2017**, *10*, 558–569.
- (7) Michaels, W.; Zhao, Y.; Qin, J. Atomistic Modeling of PEDOT:PSS Complexes II: Force Field Parameterization. *Macromolecules* **2021**, *54*, 5354–5365. Publisher: American Chemical Society.
- (8) Nyrkova, I. A.; Semenov, A. N.; Joanny, J.-F.; Khokhlov, A. R. Highly Anisotropic Rigidity of "Ribbon-like" Polymers: I. Chain Conformation in Dilute Solutions. *J. Phys. II* **1996**, *6*, 1411–1428. Publisher: EDP Sciences.
- (9) Nyrkova, I. A.; Semenov, A. N.; Joanny, J.-F. Highly Anisotropic Rigidity of "Ribbon-Like" Polymers: II. Nematic Phases in Systems between Two and Three Dimensions. *J. Phys. II* **1997**, *7*, 825–846. Publisher: EDP Sciences.
- (10) Everaers, R.; Bundschuh, R.; Kremer, K. Fluctuations and Stiffness of Double-Stranded Polymers: Railway-Track Model. *Europhys. Lett.* **1995**, *29*, 263–268. Publisher: IOP Publishing.
- (11) Liverpool, T. B.; Golestanian, R.; Kremer, K. Statistical Mechanics of Double-Stranded Semiflexible Polymers. *Phys. Rev. Lett.* **1998**, *80*, 405–408. Publisher: American Physical Society.
- (12) Golestanian, R.; Liverpool, T. B. Statistical mechanics of semiflexible ribbon polymers. *Phys. Rev. E* **2000**, *62*, 5488–5499. Publisher: American Physical Society.
- (13) Mergell, B.; Ejtehadi, M. R.; Everaers, R. Statistical mechanics of triangulated ribbons. *Phys. Rev. E* **2002**, *66*, No. 011903. Publisher: American Physical Society.
- (14) Arinstein, A. E. Conformational statistics of ribbonlike semiflexible polymer chains. *Phys. Rev. E* **2005**, *72*, No. 051805. Publisher: American Physical Society.
- (15) King, G. W.; Hainer, R. M.; Cross, P. C. The Asymmetric Rotor I. Calculation and Symmetry Classification of Energy Levels. *J. Chem. Phys.* **1943**, *11*, 27–42. Publisher: American Institute of Physics.
- (16) Alim, K.; Frey, E. Fluctuating semiflexible polymer ribbon constrained to a ring. *Eur. Phys. J. E* **2007**, *24*, 185–191.
- (17) Zhao, S.; Zhang, S.; Yao, Z.; Zhang, L. Equilibrium conformation of polymer chains with noncircular cross section. *Phys. Rev. E* **2006**, *74*, No. 032801. Publisher: American Physical Society.
- (18) Marko, J. F.; Siggia, E. D. Bending and twisting elasticity of DNA. *Macromolecules* **1994**, 27, 981–988. Publisher: American Chemical Society.
- (19) Panyukov, S.; Rabin, Y. Fluctuating filaments: Statistical mechanics of helices. *Phys. Rev. E* **2000**, *62*, 7135–7146. Publisher: American Physical Society.

- (20) Rappaport, S. M.; Rabin, Y. Differential geometry of polymer models: worm-like chains, ribbons and Fourier knots. *J. Phys. A: Math. Theor.* **2007**, *40*, 4455.
- (21) Tinkham, M. Group Theory and Quantum Mechanics; Dover Publications, 1964.
- (22) Landau, L. D.; Lifshitz, E. M. Mechanics; Butterworth-Heinemann, 1976.
- (23) Feynman, R. P.; Hibbs, A. R.; Styer, D. F. Quantum Mechanics and Path Integrals; Courier Corporation, 2010.
- (24) Zinn-Justin, J. Quantum Field Theory and Critical Phenomena; Oxford Science Publications, 1996.
- (25) Spakowitz, A. J.; Wang, Z.-G. Exact Results for a Semiflexible Polymer Chain in an Aligning Field. *Macromolecules* **2004**, *37*, 5814–5823. Publisher: American Chemical Society.
- (26) Chandrasekhar, S. Statistic problems in physics and astronomy. Rev. Mod. Phys. 1943, 15, 1.
- (27) Hiemenz, P. C.; Lodge, T. P. Polymer Chemistry, 2nd ed.; Taylor & Francis, 2007.
- (28) Spakowitz, A. J.; Wang, Z.-G. Semiflexible polymer solutions. I. Phase behavior and single-chain statistics. *J. Chem. Phys.* **2003**, *119*, 13113–13128. Publisher: American Institute of Physics.
- (29) Friedowitz, S.; Salehi, A.; Larson, R. G.; Qin, J. Role of electrostatic correlations in polyelectrolyte charge association. *J. Chem. Phys.* **2018**, *149*, No. 163335. Publisher: American Institute of Physics.
- (30) Adhikari, S.; Leaf, M. A.; Muthukumar, M. Polyelectrolyte complex coacervation by electrostatic dipolar interactions. *J. Chem. Phys.* **2018**, *149*, No. 163308. Publisher: American Institute of Physics.